ACS Catalysis
Research Article
pubs.acs.org/acscatalysis

Solar Hydrogen Production by Plasmonic Au−TiO_2 Catalysts: Impact of Synthesis Protocol and TiO_2 Phase on Charge Transfer Efficiency and H_2 Evolution Rates

Jacqueline B. Priebe,[§] Jörg Radnik, Alastair J. J. Lennox, Marga-Martina Pohl, Michael Karnahl,[†]
Dirk Hollmann, Kathleen Grabow, Ursula Bentrup, Henrik Junge, Matthias Beller, and Angelika Brückner*

Leibniz-Institut für Katalyse e.V. an der Universität Rostock, Albert-Einstein-Straße 29a, 18059 Rostock, Germany

S *Supporting Information*

ABSTRACT: The activity of plasmonic Au−TiO_2 catalysts for solar hydrogen production from H_2O/MeOH mixtures was found to depend strongly on the support phase (anatase, rutile, brookite, or composites thereof) as well as on specific structural properties caused by the method of Au deposition (sol-immobilization, photodeposition, or deposition−precipitation). Structural and electronic rationale have been identified for this behavior. Using a combination of spectroscopic in situ techniques (EPR, XANES, and UV−vis spectroscopy), the formation of plasmonic Au particles from precursor species was monitored, and the charge-carrier separation and stabilization under photocatalytic conditions was explored in relation to H_2 evolution rates. By in situ EPR spectroscopy, it was directly shown that abundant surface vacancies and surface OH groups enhance the stabilization of separated electrons and holes, whereas the enrichment of Ti^{3+} in the support lattice hampers an efficient electron transport. Under the given experimental conditions, these properties were most efficiently generated by depositing gold particles on anatase/rutile composites using the deposition−precipitation technique.

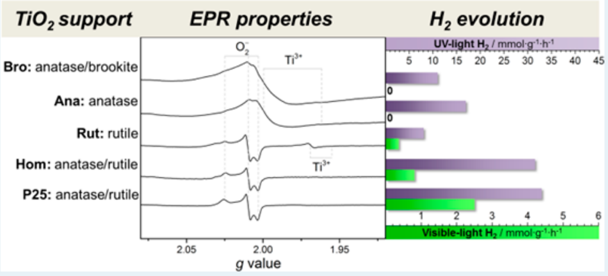

KEYWORDS: *photocatalysis, titanium dioxide, in situ spectroscopy, surface plasmon resonance, hydrogen generation*

1. INTRODUCTION

The sustainable generation of energy carriers from nonfossil resources (e.g., hydrogen production by photocatalytic water splitting) is one of the most important future challenges. For large-scale applications, catalysts are desired that work efficiently with solar radiation containing about 50% visible light alongside a small contribution of UV light, both of which can be converted into chemical energy.[1] Unfortunately, the most effective (pristine) semiconductor-based photocatalysts of the first generation, such as ZnS and $NaTaO_3$, can harvest only UV light because of their large band gaps.[2] This is also true for pristine TiO_2, which still belongs to the most active and extensively studied materials for photocatalytic reactions promoted by UV light. Therefore, much effort has been focused on the development of second-generation catalysts with higher visible-light response. One major approach has been the doping of semiconductors (especially TiO_2) with other anions (e.g., N^{3-}, C^{4-})[3] or cations (e.g., Sb^{5+}, Cr^{3+}, Fe^{3+}, V^{4+}, Mo^{5+}).[4] However, this has been done with limited success because it often leads to fast recombination of the photoinduced charge carriers as a result of the higher concentration of defects that act as favorable recombination centers.[5] Therefore, Serpone et al. pointed out that there is an urgent need for new approaches in the field of efficient catalyst design for environmental photocatalysis.[6] New third-generation photocatalysts must also allow electron−hole pair formation under visible light and simultaneously suppress charge carrier recombination to enhance the quantum yield.

Recently, the integration of metal particles exhibiting surface plasmon resonance (SPR) phenomena (e.g., Au) into conventional semiconductors, such as TiO_2, has emerged as a promising entrance to visible-light-active photocatalysts for many applications, such as decomposition of organic pollutants[7] and selective oxidation and reduction reactions of organic compounds[8] as well as for hydrogen generation from aqueous alcoholic solutions.[9] However, especially in the latter case of photocatalytic proton reduction by use of sacrificial reductants such as methanol, H_2 evolution rates of plasmonic Au−TiO_2 catalysts under visible light are still much lower than under UV light. Detailed investigations of structure−reactivity relationships, which could shine light on the influence of catalyst support properties and synthesis procedures, have been widely neglected. However, such knowledge will be very helpful for future rational catalyst design beyond trial and error.

In our recent work, we have demonstrated that in situ EPR spectroscopy is a powerful tool for unraveling mechanisms of photocatalytic water reduction in both homogeneous[10] and heterogeneous catalytic systems.[11] In the latter case, wave-

Received: November 19, 2014
Revised: February 19, 2015
Published: February 20, 2015

DOI: 10.1021/cs5018375
ACS Catal. 2015, 5, 2137−2148

length-dependent in situ EPR measurements on Au−TiO_2 confirmed an SPR-promoted direct electron transfer from the noble metal into the TiO_2 conduction band as being crucial for visible-light activity in photocatalytic hydrogen production. It is well-known that photocatalytic proton reduction activities of Au−TiO_2 catalysts differ strongly, depending on the nature of the TiO_2 support,[12] as well as on the method used for depositing Au particles on the support surface.[13] The reasons for these differences are still poorly understood, yet they might be related to the efficiency of charge separation, transport, and stabilization in the differently prepared catalysts. Therefore, it is the aim of this work to elucidate preferentially by in situ EPR spectroscopy in combination with XANES and UV−vis spectroscopy how charge transfer and formation of photoexcited species in Au−TiO_2 catalysts are governed by the Au deposition method as well as by the phase structure of the TiO_2 support. To this end, five different TiO_2 supports and three different Au deposition methods have been explored.

2. EXPERIMENTAL SECTION

2.1. Catalyst Preparation. Au−TiO_2 catalysts with an anticipated gold content of 1 wt % were prepared using various support materials: two different mixtures of anatase and rutile (P25, anatase/rutile = 85:15, Evonik, S_{BET} = 50 m^2 g^{-1}; and Hombikat, "Hom", anatase/rutile = 87:13, Aldrich, S_{BET} = 55 m^2 g^{-1}), a pure anatase phase (Ana, Sachtleben E3−588−321−006, S_{BET} = 70 m^2 g^{-1}), a pure rutile phase (Rut, Sachtleben E3-583-141-005, S_{BET} = 96 m^2 g^{-1}). An anatase/brookite mixture (Bro, anatase/brookite = 85:15, S_{BET} = 77 m^2 g^{-1}) was prepared as described elsewhere (see Supporting Information).[14]

Deposition of gold nanoparticles onto TiO_2 was carried out using different methods. Each Au deposition procedure was followed by washing with 500 mL distilled water and drying for 12 h at 100 °C. (a) Sol immobilization (denoted by -SIM) was conducted by adding an aqueous solution of poly(vinyl alcohol) (PVA) (1.2 mL, 1 wt % sol., Merck Chemicals) to $HAuCl_4·3H_2O$ dissolved in 5 mL distilled H_2O (10.1 mM). A dark sol was formed by dropwise addition of a freshly prepared $NaBH_4$ solution (2.5 mL, 0.1 M, Aldrich, >96%). After 30 min, the TiO_2 support (1.0 g) was added and the suspension was further stirred for 12 h at 25 °C. (b) The photodeposition procedure was applied only to the P25 support material. P25 (1.0 g) was added to 100 mL of methanol, and the suspension was flushed with argon in a Schlenk tube to remove oxygen as a potential electron acceptor. Prereduction occurred by irradiation with a 300 W Xe lamp (LOT Oriel) for 20 min, whereby the color of the precipitate changed to blue, indicating the formation of Ti^{3+}. An aqueous solution of $HAuCl_4·3H_2O$ (0.53 mL, 0.1 M) was dropped into this suspension, which was then stirred for an additional 2 h at 25 °C prior to filtration. The sample is denoted by AuP25-PD. (c) The deposition−precipitation (denoted by -DP) procedure was carried out by heating an aqueous solution of $HAuCl_4·3H_2O$ (50 mL, 5 mM, Aldrich) to 70 °C. A NaOH solution (10.5 mL, 0.1 M) was added dropwise to adjust the pH to around 7. A 10.8 mL portion of the Au-containing solution was added to 96.8 mL distilled water and stirred for 15 min at 70 °C prior to the addition of the TiO_2 support (1.0 g). The resulting suspension was stirred for an additional 1 h at 70 °C and then for 1 h at 25 °C. The effect of a prolonged reaction time for the deposition−precipitation procedure was investigated by extending the stirring time of the suspension at 25 °C from 1 to 12 h (denoted by -DP12). All catalyst obtained after procedures a, b, and c were used for catalytic and spectroscopic experiments in their as-prepared form, that is, without calcination at elevated temperature. In addition, portions of the dried AuP25-DP catalyst were calcined at 200, 400, and 600 °C (5 K/min, 2 h) in flowing air (denoted by AuP25-DP200, AuP25-DP400, AuP25-DP600, respectively) with the aim to influence the Au particle size.

2.2. Catalyst Characterization. The amount of deposited gold was determined by ICP−OES using a Varian 715-ES ICP-emission spectrometer and ICP Expert software. The specific surface area (S_{BET}) of the catalysts was analyzed using a BELSORP mini device. Prior to analysis, the catalyst was dried under vacuum for 2 h at 150 °C to remove physisorbed water. Transmission electron microscopy (TEM) investigations were conducted at 200 kV using a JEM-ARM200F (JEOL) instrument. The microscope was equipped with a JED-2300 (JEOL) energy-dispersive X-ray spectrometer for chemical analysis. HAADF imaging was operated with a spot size of 5 c (ca. 0.15 nm) and a 30 μm condenser aperture. Prior to TEM analysis, the sample was deposited on a carbon-supported Cu grid (mesh 300). X-ray photoelectron spectra (XPS) were recorded using a VG ESCALAB 220iXL instrument with monochromatic Al Kα radiation (E = 1486.6 eV). Peaks were fitted by Gaussian−Lorentzian curves after Shirley background subtraction with a mean error in binding energies of ±(0.1−0.2) eV. The electron binding energy was referenced to the adventitious carbon with C 1s peak at 284.8 eV. For quantitative analysis, the peak areas were determined and divided by the element-specific Scofield factor and the analyzer-depending transmission function.

2.3. In Situ Spectroscopic Studies. UV−vis diffuse reflectance spectra were recorded with an Avantes 45° optical probe connected to an Avantes AvaSpec-2048 UV−vis spectrometer either of the pure catalyst or in a suspension of 20 mg catalyst in 2 mL H_2O/MeOH under UV−vis irradiation. In situ EPR spectra in X-band were recorded at room temperature by a Bruker EMX CW-microspectrometer in special "home-made" flow cells while passing a carrier gas stream saturated with water and methanol (He 30 mL/min with 5% H_2O/MeOH at a volume ratio of 1:1) through the catalyst. An ER 4119HS-WI high-sensitivity optical resonator with a grid in the front side enabled irradiation of the samples with a 300 W Xe-arc lamp (LOT Oriel), equipped with an optical cutoff filter (LOT Oriel GG420). g values were calculated using the equation $h\nu = g\beta B_0$ with B_0 and ν being the resonance field and frequency, respectively. The g values were calibrated using a DPPH standard (g = 2.0036 ± 0.00004). The X-ray absorption experiments were carried out at the μ-spot beamline at the synchrotron storage ring BESSY II of the Helmholtz Center for Materials and Energy in Berlin. All samples were filled in a quartz glass capillary with 1 mm diameter and a wall thickness of 0.01 mm. The fluorescence of the Au Lα was detected using a silicon drift detector. For irradiation with light, the same setup was used as described for the EPR measurements.

2.4. Photocatalytic Tests. All catalytic experiments were carried out under argon atmosphere with freshly distilled solvents. In a standard reaction, a double-walled and thermostatically controlled reaction vessel was connected to an automatic gas buret (conditions: 50 mg catalyst in 10 mL MeOH/H_2O (1:1) with 7.2 W Hg vapor light irradiation (Lumatec Superlite 400), T = 25 °C). Further details on the equipment and the experimental setup have been published previously.[15] In most cases, the gas evolution was recorded first under UV−vis light (320−500 nm filter) for 3 h and subsequently under visible light (400−700 nm filter) for an additional 3 or 21 h. The radiation spectrum of each filter is shown in Figure S1. For very active samples (AuP25-DP and AuHom-DP), the visible-light activity was measured separately for 21 h. Exemplary H_2-evolution curves are depicted in Figures S2 and S10. After each reaction, a gas sample was taken for GC analysis to determine the composition of the evolved gases (GC HP 6890N, carboxen 1000, TCD, external calibration). The variation of the hydrogen volumes for repeat experiments was between 5 and 25%, including the error of the measurement setup itself as well as the reproducibility of the preparation method of the catalysts. For AuP25-SIM as well as for tests of AuP25-DP and AuP25-DP200 with visible light, higher variations were observed, which was probably caused by unspecific structural variations resulting from the repeated synthesis procedure.

3. RESULTS AND DISCUSSION

3.1. Influence of the Gold Deposition Method. For depositing catalytically active noble-metal nanoparticles onto the surface of metal oxide supports, different methods, such as impregnation (IMP), deposition−precipitation (DP), photodeposition (PD) or sol-immobilization (SIM) are described.[16] The IMP procedure, in which primarily $HAuCl_4$ crystallites are dispersed on the support surface, is known to be less suitable for the deposition of Au on TiO_2 because it leads to pronounced agglomeration of the Au particles by the chloride ions.[17] Therefore, we focused on SIM, PD, and DP methods to deposit 1 wt % Au nanoparticles on the support to be used as catalysts for photocatalytic proton reduction in the presence of methanol as the sacrificial reductant. P25 (anatase/rutile composite) was selected as the support material to study the influence of the different Au deposition methods.

Table 1. Au Loadings and Particle Sizes As Well As Catalytic Activities of AuP25 Prepared by Different Au Deposition Procedures

			H_2 evolution rate, mmol g^{-1} h^{-1}	
cat., AuP25-	Au loading, wt %	d_m (Au), nm	UV−vis[a]	vis[b]
SIM	0.94	8.7	24	1.2
PD	0.46	41	5.1	0.42
DP	0.93	1.1	33	2.4
DP12	0.35		3.4	0.25

[a]UV−vis: 320−500 nm filter. [b]Vis: 400−700 nm filter (Figure S1).

3.1.1. Catalyst Characterization and Performance. Table 1 summarizes the Au loading (determined by ICP−OES) and the mean Au particle size (based on TEM analysis) obtained by each deposition method along with the respective H_2 evolution rates under irradiation with UV−vis (320−500 nm) and visible light (400−700 nm). By use of SIM and DP methods, the Au loading onto TiO_2 was almost 1 wt %, but only 0.46 wt % Au could be deposited by PD. Among the samples prepared by the three different methods, sample AuP25-PD showed the lowest hydrogen evolution under UV and visible light, whereas sample AuP25-DP was most active under both conditions (Table 1, Figure S2). However, this sample was also more sensitive against the specific experimental conditions of Au deposition. This is clearly illustrated by comparing samples AuP25-DP and AuP25-DP12. The latter was prepared with 12 h of reaction time instead of 1 h at 25 °C. In this case, only 0.35 wt % of gold could be deposited on the support, probably because of a related surface modification of TiO_2 resulting in lower Au binding ability. The photocatalytic activity decreased strongly by a factor of 10 to only 3.4 $mmol_{H_2}$ g^{-1} h^{-1} under UV and to 0.25 $mmol_{H_2}$ g^{-1} h^{-1} under visible light conditions (Table 1, Figure S2).

As far as the source of the formed H_2 is concerned, it cannot be excluded that a part of the protons stems from MeOH; However, this should be only a minority because Bahnemann et al.[18] have clearly shown by isotopic labeling studies that H_2 is predominantly formed from water, not from methanol, because D_2, not H_2, was the major product evolved from CH_3OH/D_2O mixtures. The formation of H_2 by abstraction of H from the methanol CH_3 group might be highly unprobable because it was shown previously that the H_2 production rates in CH_3OH/H_2O and CD_3OH/H_2O mixtures were almost the same.[15] This also holds true for the pure thermocatalytic decomposition of MeOH because no H_2 formation has been detected in the dark.

Scheme 1. Processes Induced by UV and Visible Light in Au−TiO_2 in a H_2O/MeOH Mixture[a]

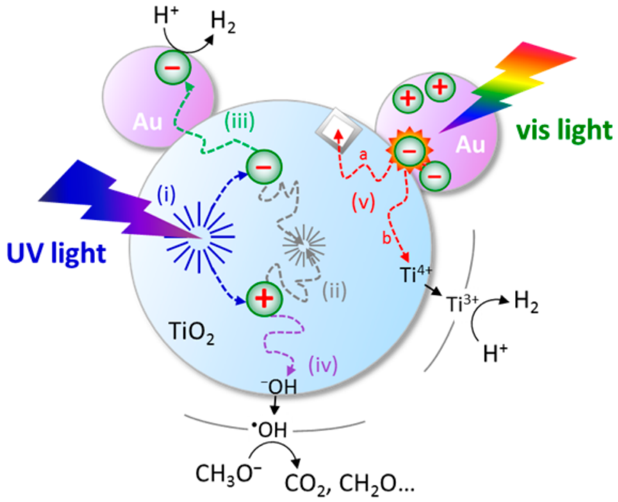

[a]Steps: (i) electron−hole pair formation by band-gap excitation of TiO_2; (ii) recombination of charge carriers, for example, at defect sites; (iii) electron transfer into the Au particle and subsequent proton reduction; (iv) hole trapping at surface-bound OH groups with proximate MeOH decomposition; and (v) transfer of SPR-excited Au electrons into TiO_2 and their trapping at surface oxygen vacancies (a) or lattice-Ti^{4+} (b) prior to proton reduction.

As demonstrated in our previous work, two different electron transfer mechanisms in Au−TiO_2 for proton reduction have been distinguished, depending on the excitation wavelength (Scheme 1).[11a] Under UV light, valence band electrons are excited to the conduction band of TiO_2 (i) and quickly transferred to Au with its lower Fermi level (ii), whereby the recombination of charge carriers (iii) is suppressed. The remaining holes in the valence band oxidize the sacrificial reactant MeOH either directly or indirectly after trapping at surface-bound OH-groups (iv), while the electrons can effectively reduce the protons at the surface of the metal particles. The smaller the Au particles, that is, the higher the exposed Au surface, the more active sites can act as electron traps and proton reduction centers. Furthermore, smaller Au particles shift the Fermi level of Au−TiO_2 composites more negatively than large particles, which enhances the separation of the UV-light-excited electrons.[19] Thus, the UV light photoactivity should be influenced mainly by the Au size distribution of the catalyst, although this seems to be not the only crucial property, as discussed below for a series of DP samples calcined at different temperatures (section 3.1.3).

In contrast, the opposite trend in Au particle size is important for high visible light activity mediated by the SPR effect. Here, the Au particles must not be smaller than a critical minimum size because SPR absorption starts to be detectable only at a cluster size above 2 nm, when the collective electron oscillations give rise to plasmon polaritons.[19] Moreover, the strength of these SPR oscillations increases with the Au particle size,[20] implying that larger particles might lead to higher H_2 evolution rates. This has been confirmed by Wei et al., who did not observe SPR-induced H_2 generation for small Au particles (4.4 nm) but did for particles of 37 nm.[20] Because the SPR-mediated transfer of Au conduction electrons into the conduction band of TiO_2 occurs via an excited "hot-electron" state[21] (Scheme 1, v), it should be promoted by strong metal−support interaction (SMSI effect).

Figure 1 depicts the optical absorption bands arising from surface plasmon resonance of the Au−TiO_2 catalysts prepared by different deposition methods. The position and intensity of the SPR band depend on the Au particle size and shape.[22] Small particles give rise to higher collective oscillation frequencies of the conduction electrons by interaction with the incident light so that the maxima of SPR bands are observed at lower wavelengths. The band positions of the AuP25-SIM (λ_{max} = 545 nm) and AuP25-PD (λ_{max} = 565 nm) samples indicate that SIM leads to smaller particles than the PD procedure, probably because of the use of poly(vinyl alcohol) (PVA) as a particle stabilizer. It is known that PVA promotes controlled particle growth by surrounding the Au nanodots, which inhibits the agglomeration of individual Au particles to larger clusters. In this context, the PVA/Au ratio influences the Au particle size distribution, as demonstrated elsewhere.[23] In contrast, the Au particles formed by PD are not growth-protected, and the incident light can stimulate the particle movement.[24] So coagulation with time is likely. Transmission electron microscopy images confirm this assumption, showing mean particle sizes of 8.7 nm for AuP25-SIM and 41.8 nm for AuP25-PD (Figure 2 a, b).

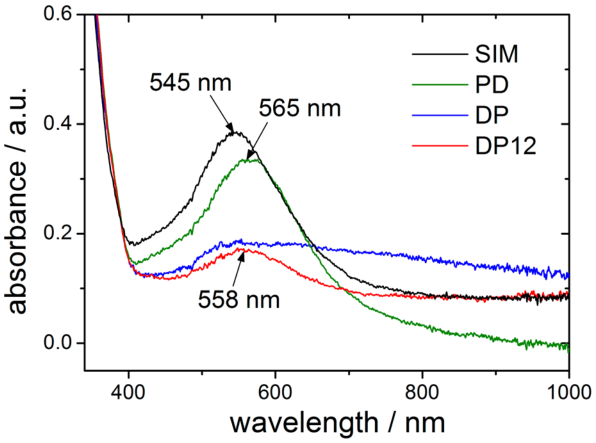

Figure 1. Au-SPR absorption bands of AuP25 catalysts prepared by different Au deposition methods.

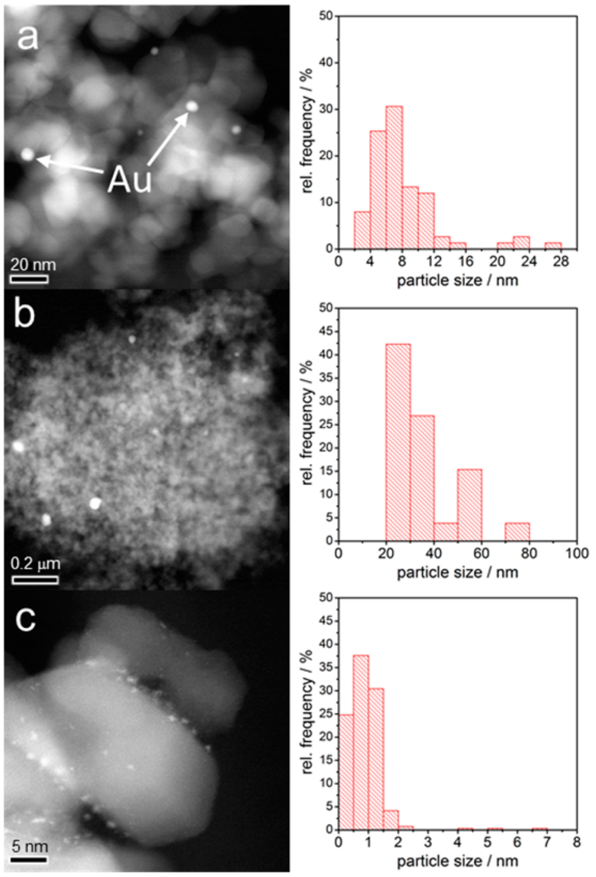

Figure 2. HAADF-TEM images and Au particle-size distribution of samples prepared by (a) sol-immobilization (AuP25-SIM), (b) photodeposition (AuP25-PD), and (c) deposition−precipitation (AuP25-DP).

Wei et al. reported that the visible-light activity of Au−TiO_2 catalysts can result from a residual TiO_2 absorption when filters >400 nm were applied and is not necessarily solely based on the plasmonic excitation of Au electrons.[20] As seen by the radiation spectrum of the integrated vis light filter of our Hg light source (Figure S1b), a small UV-light contribution cannot be excluded in accounting for the vis-H_2 evolutions given in Table 1. Atmospheric sunlight also contains a few percent of UV radiation, and thus, the overall goal should be to find catalysts working best under solar excitation. However, to study the extent of pure plasmon-induced H_2 evolution, selected catalysts were tested employing an additional external filter >420 nm (Table S1). We observed a significant amount of H_2 (15 μmol after 26 h, Table S1) evolved over AuP25-SIM, whereas AuP25-DP12 was almost inactive under these conditions, as well (Table S1, experiments II and III). Moreover, in situ FTIR spectra of AuP25-SIM in H_2O/MeOH show similar bands under irradiation with UV−vis and visible light >420 nm but of much lower intensity for the latter conditions (Figure S7). These results strongly suggest a weak SPR-induced activity of AuP25-SIM for proton reduction, although the Au particles in this sample are 8.7 nm, significantly smaller compared with those in the active catalysts of Wei et al.[20] As pointed out below and in our previous study,[11a] evidence for an SPR-mediated direct electron transfer from Au to TiO_2 being responsible for the vis activity of AuP25-SIM was provided by EPR spectroscopy.

The SPR band of AuP25-DP differs strongly from those of AuP25-SIM and AuP25-PD (Figure 1). In addition to lower absorbance, indicating a lower number of SPR-active particles, the absorption band extends to the higher wavelength range, showing no clear maximum. TEM analysis revealed the formation of very small Au species with a mean Au diameter of 1.1 nm (Figure 2c). As mentioned above, surface plasmon resonance absorption starts to be detectable only at a cluster size above 2 nm.[19] Thus, the low SPR absorption might be due to the very small mean Au diameters in AuP25-DP. Moreover, the XPS Au 4f peaks from sample AuP25-DP are shifted to higher binding energies (84.3 eV, Figure 3, Table 2) compared with values typically found for reduced Au^0.[25] This may be due to two reasons: (i) final state effects resulting from the high dispersion (very small particles) of Au particles, as derived from TEM (Figure 2c), which may also explain the broadening of the XPS peaks;[26] and (ii) the presence of partly oxidized $Au^{\delta+}$ species,[27] which has also been confirmed by XANES data explained below. Such species can result from $Au(OH)_3$ oligomers initially formed during the DP procedure (Scheme 2).[28]

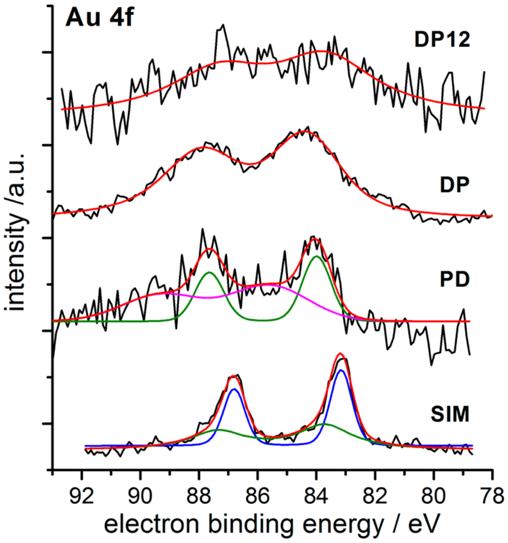

Figure 3. Au 4f XPS spectra for the AuP25 samples prepared by different deposition procedures.

Table 2. XPS Binding Energies and Assignment of AuP25 Prepared by Use of Different Au Deposition Methods

cat. AuP25-	Au, at. %	E_B (Au 4f), eV	E_B (Ti 2p), eV
SIM	0.25	83.2 (Au^0–$V^{\bullet-}$)	458.7 (Ti^{4+})
		83.7 (Au^0)	
PD	0.08	84.0 (Au^0)	457.3 (Ti^{3+})
		85.5 (Au^{3+})	458.9 (Ti^{4+})
DP	0.57	84.3 ($Au^{\delta+}$)	459.4 (Ti^{4+})
DP12	0.11	83.7 (Au^0)	457.1 (Ti^{3+})
			458.8 (Ti^{4+})

The XPS spectrum of sample AuP25-SIM in the Au 4f region can be deconvoluted into two signals (Figure 3, Table 2). The peak at 83.7 eV (green line) is in the range of reduced Au^0 formed upon treatment with $NaBH_4$.[25] The second signal at 83.2 eV (blue line) can be assigned to Au^0 bound at an O–vacancy (Au–$V^{\bullet\bullet}$).[29] It is known that oxygen vacancies, formed in TiO_2 under a reducing environment such as $NaBH_4$ solution (Scheme 2), act as Au nucleation sites.[30] The electrons initially belonging to the O^{2-} ions contribute partially to the bond formation between Au and the defect site. Thus, the binding energy of these Au–$V^{\bullet\bullet}$ states is decreased by a negative charge transfer from the defective TiO_2 surface to the Au particle.[29] For catalyst AuP25-PD, XPS analysis revealed the presence of Ti^{3+} species on the surface (Table 2, Figure S3) as a consequence of prereduction by irradiation in MeOH (acting as scavenger of positive holes). The Ti^{3+}-enriched surface is able to reduce adsorbed Au^{3+} (Scheme 2). However, as seen from the XPS data (Figures 3 and S3, Table 2), this reduction was incomplete and led to a mixture of Au^{3+}/Au^0 and Ti^{3+}/Ti^{4+}, with a rather low Au content on the surface compared with the other methods (Table 2). This fact could be a reason for its low H_2 evolution rate under UV light (Table 1, Figure S2) as a result of the lack of active sites at the surface. Furthermore, although the Au particles in AuP25-PD are of a size similar to those in the most active sample of Wei et al.[20] and exhibit a strong SPR absorption, electron transfer from Au to TiO_2 may be hindered because of these surface defects and less SMSI, causing low vis-H_2 rates.

To identify the initial oxidation state of Au as well as its changes during the photocatalytic reaction, in situ XANES measurements at the Au LIII-edge were conducted on catalysts AuP25-SIM and -DP (Figure 4). The spectrum of the as-prepared AuP25-SIM (Figure 4a, red line) is similar to that of Au foil (dashed line) and does not change upon addition of H_2O/MeOH (blue line) or under subsequent irradiation (green line), which confirms the presence of predominantly reduced Au^0 particles. In contrast, the AuP25-DP catalyst shows a prominent peak ("white line") 4 eV above the Au LIII absorption edge (Figure 4b), which is characteristic for oxidized $Au^{\delta+}$ species, in accordance with XPS data (Table 2).[31] However, when sample AuP25-DP was exposed to a H_2O/MeOH mixture, the white line disappeared, and the spectrum became similar to that of Au foil, indicating the formation of Au^0 particles already in the dark. The difference spectrum (Figure 4b) clearly illustrates this change in the oxidation state of Au. During subsequent irradiation, no significant changes are observed. A more detailed description of light-induced changes of this sample can be found in the Supporting Information. In brief, the in situ formation of equally sized and highly dispersed Au particles in the AuP25-DP may contribute to its high activity, which cannot be achieved by calcination, as shown below.

Interestingly, prolonging the deposition time in the DP method from 2 to 12 h led to an SPR band of very low intensity (Figure 1), despite the fact that Au^0 is evident from XPS analysis, although with a much lower surface concentration of only 0.11 at. % (compared to 0.57 at. % after 2 h deposition; Table 2). Furthermore, no Au species could be identified by TEM in AuP25-DP12 (not shown). A contribution of Ti^{3+} in the Ti 2p XPS spectrum for AuP25-DP12 (Table 2, Figure S3) indicates the presence of surface defect sites. In addition, its low photocatalytic H_2 evolution (Table 1, Figure S2) suggests drastic structural differences compared with the other AuP25 catalysts. On the basis of these data, it seems probable that a considerable amount of the gold is incorporated into the TiO_2 matrix via interaction of Au species with those defect sites

Scheme 2. Steps of Au Deposition Passed during Sol Immobilization (SIM), Photodeposition (PD), and Deposition–Precipitation (DP)

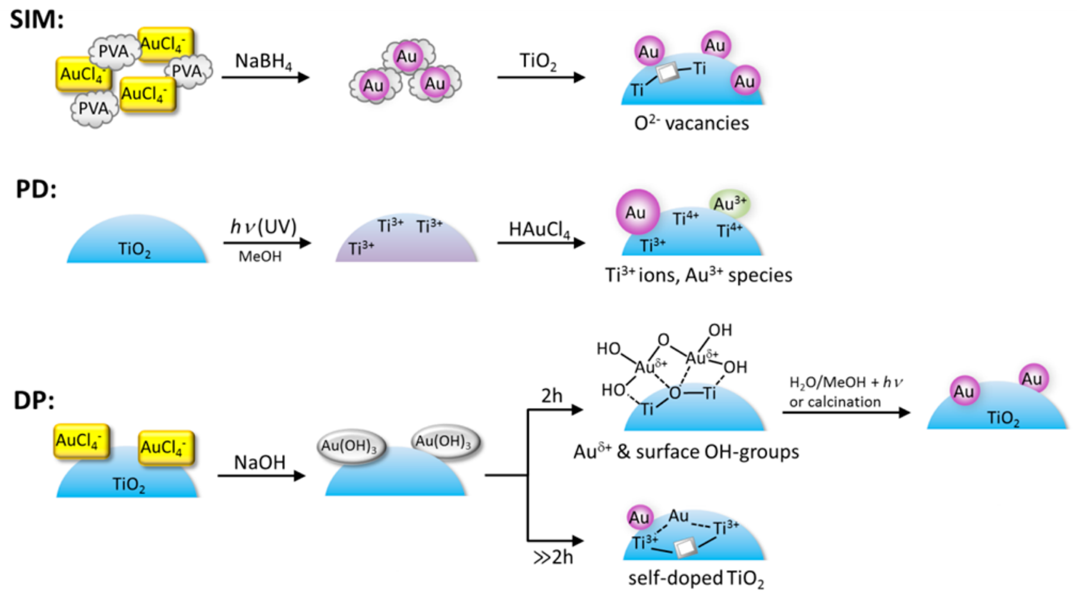

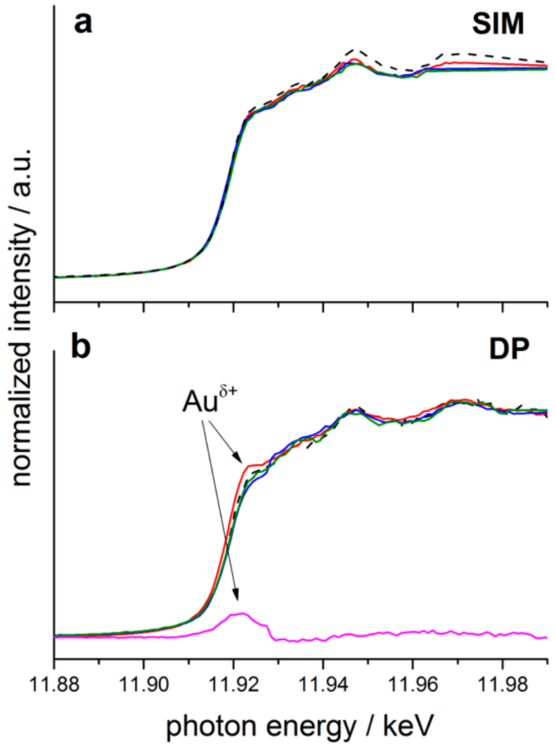

Figure 4. In situ XANES of (a) AuP25-SIM and (b) AuP25-DP starting with pure catalyst in the dark (red), after addition of a H_2O/MeOH (1:1) mixture (blue) and UV irradiation (green) compared with Au foil (black dashed line). The pink line results from subtraction of the blue from the red line and visualizes the oxidized state of Au in AuP25-DP.

(Scheme 2) and, thus, is no longer active for the catalytic reaction.

3.1.2. In Situ EPR Investigations. To explore the relationship between electronic and structural propties, the nature of photoexcited species of each catalyst upon irradiation with UV–vis light was characterized by in situ EPR spectroscopy. Moreover, their behavior upon subsequent addition of water and methanol has been analyzed (Figure 5). The room temperature EPR spectrum of the AuP25-SIM catalyst in the dark exhibits a weak signal at $g = 2.005$, which most likely arises from electrons trapped at TiO_2 oxygen vacancies (Table 3). Upon irradiation, visible light excites the SPR-promoted transfer of Au conduction electrons to the conduction band of TiO_2, from which at least some of them are further moved to and trapped at such vacancies, making them visible by EPR, as demonstrated earlier in detail (see Scheme 1, v_a).[11a] By addition of water and methanol, the electrons transferred from Au to the TiO_2 conduction band as well as to the surface vacancies (being preferable binding sites for reactants) can reduce adsorbed protons. This decreases the intensity of the EPR signal at $g = 2.005$ (Figure 5c,d; black). On the other hand, surface oxygen vacancies could also get saturated with adsorbed water molecules (hydroxyl group formation), which may block these trapping sites for Au electrons.[30]

Although for AuP25-PD and AuP25-DP, no paramagnetic species were observed in the dark, an intense EPR signal with axial symmetry below $g = 2$ was detected for AuP25-DP12, which can be assigned to Ti^{3+} (Figure 5a, red, Table 3). In the majority of cases, Ti^{3+} can be seen only at low temperature because of short spin–lattice relaxation times τ_1, which are governed by the ability of the excited spin system to dissipate its energy by interaction with vibrations (phonons) of the surrounding lattice. It has been shown that in spherical and rod-like TiO_2 particles with a curved surface and a high concentration of unsaturated Ti atoms, spin–lattice relaxation of Ti^{3+} sites is ~2 orders of magnitude slower than in well-ordered "bricklike" single crystals.[32] Accordingly, the spin–lattice relaxation rate of the Ti^{3+} sites in AuP25-DP12 may be attenuated as a result of their location near the surface, which may cause coordinative unsaturation or a distortion of the Ti–O environment leading to less effective energy dissipation via phonons. Sample AuP25-PD does not show such a Ti^{3+} EPR signal at room temperature, despite the fact that it does contain Ti^{3+}, as shown by XPS (Table 2, Figure S3). The reason may be differences in the electronic or geometric environment of the Ti^{3+} sites in sample AuP25-PD that shorten the relaxation time.

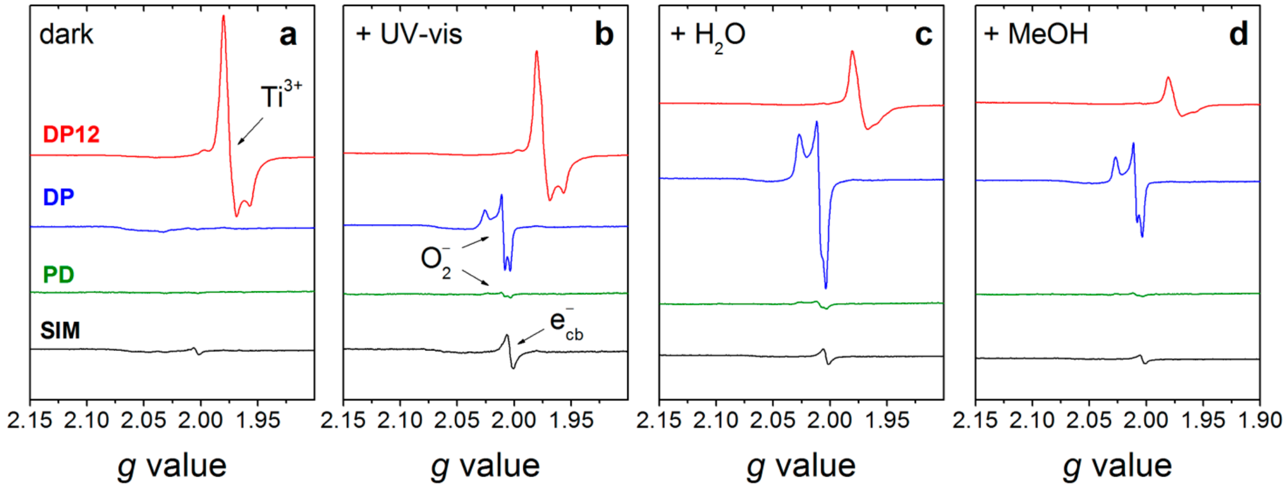

Figure 5. In situ EPR spectra of AuP25 catalysts prepared by SIM (black), PD (green), DP using a deposition time of 2 h (blue) and DP12 using a deposition time of 12 h (red). Spectra were recorded at 290 K after 20 min under the respective conditions in the dark (a) followed by UV−vis irradiation (full spectrum of Xe lamp) (b) with subsequent addition of H_2O (c) and MeOH (d).

Table 3. EPR Parameters of Detected Signals and Their Assignment Based on Literature Data

	EPR parameters		
signal/assignment	g_1	g_2	g_3
e_{cb}^-: electrons trapped at O^{2-} vacancies[11a]	2.005	2.005	2.005
Ti^{3+} (self-doped) in Au−TiO_2[33a,c]	1.975	1.975	1.957
bulk Ti^{3+} (anatase)[34]	1.990	1.990	1.962
O_2^-: superoxide radical[35]	2.026	2.010	2.003

The EPR signal intensity of this surface Ti^{3+} species was reduced upon the introduction of water and methanol, which act as charge scavengers (Figure 5c and d, red). These Ti^{3+} centers can be assigned to "self-doped" TiO_2, which is formed by partial self-reduction of lattice Ti^{4+} sites accompanied by O^{2-} vacancy formation (Scheme 2).[33] In contrast to literature reports on the beneficial effects of self-doped TiO_2 for photocatalytic reactions,[33a,b] the activity of the Ti^{3+}-containing catalyst AuP25-DP12 decreased dramatically compared with AuP25-DP (Table 1, Figure S2, Table S1). This is probably due to the lower capability of charge transfer to (under UV light) and from (under visible light) the Au particles and a lower number of active sites at the surface.

In contrast, the EPR spectrum of the highly active AuP25-DP catalyst prepared by short-term deposition−precipitation does not show any signal in the dark, but an intense rhombic species with characteristic *g* values of surface-bound superoxide radicals ($O_2^{\bullet-}$) under irradiation (Figure 5b blue, Table 3). In principle, there are two possible mechanisms to form $O_2^{\bullet-}$ on TiO_2 under irradiation: electron-mediated or hole-mediated. In the first case, traces of molecular oxygen in the helium flow may capture electrons to form adsorbed superoxide radicals because the redox potential $E^0(O_2/O_2^{\bullet-})$ is slightly more positive (−0.33 V vs NHE)[36] than the TiO_2 conduction band potential (−0.45 V for anatase):[37]

$$TiO_2 + h\nu \rightarrow TiO_2(h_{vb}^+) + TiO_2(e_{cb}^-) \tag{1}$$

$$TiO_2(e_{cb}^-) + O_2 \rightarrow TiO_2 + O_2^{\bullet-} \tag{2}$$

However, this origin for the $O_2^{\bullet-}$ species is not likely because those signals should then appear in all spectra. On the other hand, because the surface of AuP25-DP is populated by OH^- species as derived from the FTIR spectra (Figure S8), fast trapping of positive holes at these OH^- groups may lead to the formation of hydroxyl radicals (Scheme 1, iv), the redox potential of which is more negative ($E^0(OH^\bullet/OH^-)$ = 1.90 V)[38] than the valence band potential of TiO_2(E_{vb} = 2.66 V).[39] A feasible hole-mediated reaction sequence was proposed by Howe et al. for hydrated anatase,[35] in which $OH^\bullet$ radicals quickly recombine to hydrogen peroxide, which is further converted to hydroperoxyl radical upon reaction with another trapped hole ($E^0(H^+, HO_2^\bullet/H_2O_2)$ = 1.44 V).[40] Bound to metal oxides, these radicals quickly deprotonate at the basic centers to form $O_2^{\bullet-}$:[41]

$$TiO_2(h_{vb}^+) + OH^- \rightarrow TiO_2 + OH^\bullet \tag{3}$$

$$2OH^\bullet \rightarrow H_2O_2 \tag{4}$$

$$OH^\bullet + H_2O_2 \rightarrow HO_2^\bullet + H_2O \tag{5}$$

$$TiO_2{-}HO_2^\bullet \rightarrow H^+ + TiO_2 - O_2^{\bullet-} \tag{6}$$

This mechanism is supported by the increasing signal intensity after addition of H_2O, which should create more surface-bound hydroxyl groups and, thus, more primary trapping sites for h_{vb}^+. Furthermore, the decrease in the $O_2^{\bullet-}$ signal upon adding the hole scavenger MeOH indicates a consumption of trapped holes (Scheme 1, (iv)). The efficient trapping of holes by surface-bound hydroxyls, leading to $O_2^{\bullet-}$ species in the absence of any reactant, and their consumption by methanol may hinder them from recombination with the electrons. Furthermore, the oxidation of MeOH was shown to proceed faster indirectly by hydroxyl-trapped holes than through a direct mechanism.[42] Given the fact that the DP method reveals catalysts of high surface−OH coverage in the as-prepared state, we think that this may explain the higher activity of sample AuP25-DP compared with sample AuP25-SIM (Table 1).

In the less active sample AuP25-PD, an $O_2^{\bullet-}$ EPR signal is hardly observed under UV−vis irradiation and by addition of water (Figure 5b,c; green). This may be due to a less effective charge-carrier separation, which results from the inhibiting structural characteristics created during the Au deposition procedure, as described above. Therefore, fewer positive holes get trapped at surface-bound hydroxyl groups capable of promoting the formation of $O_2^{\bullet-}$ according to eqs 3–6. The above-discussed results illustrate once more the unique potential of in situ EPR for dedicated mechanistic investigations, as demonstrated recently.[11a] The technique is able to visualize both formation and stabilization of positive holes mediated by OH^- surface species, as well as SPR-promoted transfer and trapping of Au conduction electrons, which depend on the particular surface properties created by different Au deposition methods.

3.1.3. Effect of Calcination Temperature on AuP25-DP. As illustrated in Figures 4 and S4b, the gold component in the as-synthesized AuP25-DP is present as partially oxidized $Au(OH)_x$ species, which are reduced to Au^0 in the reaction mixture (H_2O/MeOH). Well-defined Au^0 particles can also be obtained by controlled thermal pretreatment in which the chosen temperature has a crucial influence because it affects the Au particle growth, which is usually accompanied by a shift of the SPR band position to higher wavelengths.[43] Figure 6 depicts the UV–vis absorption spectra of AuP25-DP (uncalcined) and samples AuP25-DP200, AuP25-DP400, and AuP25-DP600, calcined at 200, 400, and 600 °C, respectively. Although the samples treated at 200 and 400 °C exhibit similar SPR band positions and shapes, TEM analysis revealed the largest mean Au-particle size in the AuP25-DP200 catalyst (Figure 7, Table 4), whereas AuP25-DP400 and AuP25-DP600 showed almost the same Au particle size. Nevertheless, these two samples differ significantly in their H_2 evolution rates (Table 4). This suggests that other effects (discussed below) influence the catalytic activity, as well.

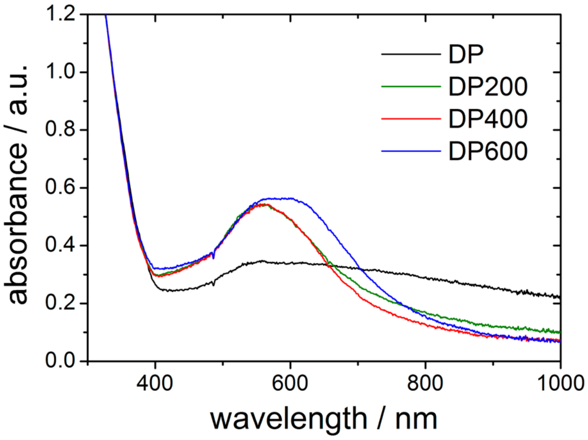

Figure 6. UV–vis absorption spectra of AuP25-DP uncalcined (DP, black) as well as calcined at 200 (DP200, green), 400 (DP400, red), and 600 °C (DP600, blue).

As seen from XPS analysis, low temperature treatment at 200 °C did not change the Au states significantly (Table 4), indicating that partially oxidized $Au^{\delta+}$ species are still present. In principle, during the Au^0-particle-forming process, the surface-bound $Au(OH)_3$ oligomers become dehydrated and thus agglomerate to larger Au_2O_3 units, which in turn are decomposed to Au^0 and O_2 at sufficiently high temperatures.[44] Most probably, in addition to SPR-active Au^0 particles originating from the larger Au_2O_3 units, in AuP25-DP200, there were also nonreduced Au species present in larger agglomerates than in the uncalcined sample, leading to such a strong activity loss under UV–vis and visible light (Table 4). Treatment at higher temperature (>400 °C), however, stimulates movement and preferential deposition of Au particles at the anatase/rutile interface.[45] Furthermore, it promotes particle growth and enhances the metal–support interaction.[46] Although these effects may barely play a role in single-phase materials, such as pure anatase or pure rutile, they could promote charge transfer across the anatase/rutile interface in P25. Previous EPR studies[47] indicated that better charge separation is achieved in P25 through a transfer of photoexcited electrons from rutile to anatase, the conduction band potential of which is below that of rutile as derived by recent XPS and DFT investigations.[48]

The in situ EPR spectra demonstrate nicely the effect of temperature treatment on the ability of charge separation. The less active catalysts treated at 200 and 400 °C rarely show any indication for superoxide radicals (reflecting trapped holes) at $T = 290$ K (Figure 8), whereas the more active samples DP and DP600 exhibit intense $O_2^{\bullet-}$ signals. Moreover, light-induced Ti^{3+} species have been detected in the bulk of the TiO_2 phases

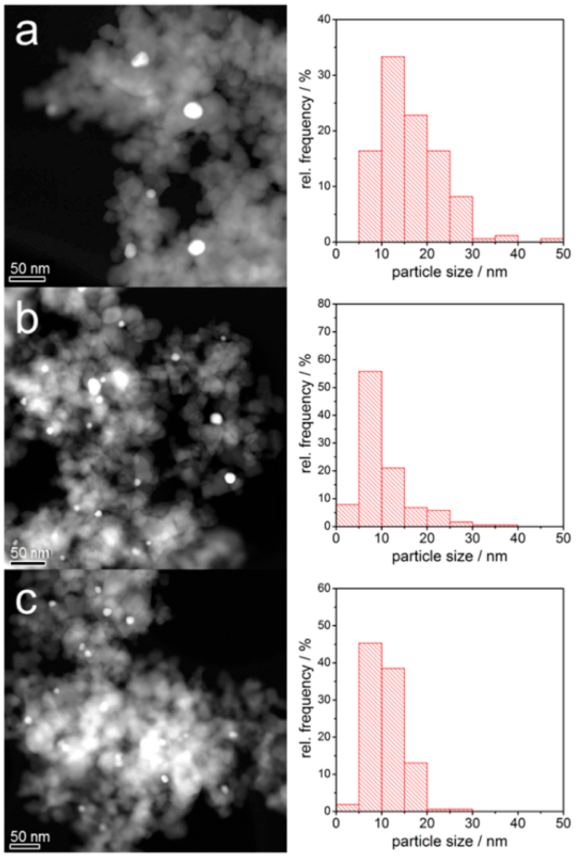

Figure 7. HAADF-TEM images and particle-size distributions of AuP25-DP calcined at (a) 200, (b) 400, and (c) 600 °C.

Table 4. Influence of Calcination Temperature on H_2 Evolution Rate, Mean Au Particle Diameter and XPS Parameters of AuP25-DP Samples

				H_2 evol. rate, mmol g^{-1} h^{-1}	
cat. AuP25-	d_m (Au), nm	Au at. %	E_B (Au 4f), eV	UV–vis	vis
DP	1.1	0.57	84.3	33	2.4
DP200	16	0.23	84.5	9.0	0.3–1.2
DP400	10			20	1.1
DP600	11	0.13	83.6	31	1.8

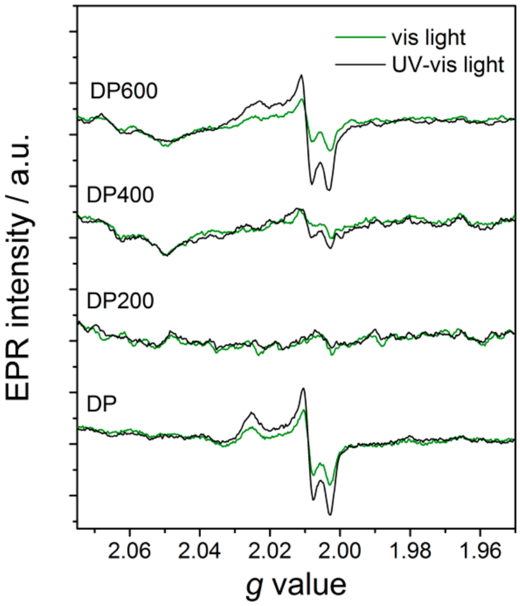

Figure 8. EPR spectra (T = 290 K) of AuP25-DP both uncalcined and calcined at 200, 400, and 600 °C after 20 min of pure visible-light ($\lambda >$ 420 nm) irradiation (green) as well as after subsequent UV−vis irradiation for an additional 20 min (black).

in samples DP200 and DP400 (Figure S9), which appear significantly less in the more active samples DP and DP600 under the same conditions. Obviously, a certain part of the photoexcited electrons in the less active samples is, rather, trapped as Ti^{3+} than being transferred to Au, possibly because of less effective metal−support interaction (SMSI) or a lower number of trapping sites, whereas the ability to generate separated charge carriers may be higher in the most active samples DP and DP600. This may lead to better activities as a result of efficient suppression of recombination processes, as discussed above. These results suggest that a proper match of the electronic and surface structure of the support material with the Au charge donation and take-up abilities is required for high catalytic activity. Therefore, the influence of the different support materials on the H_2 evolution was investigated.

3.2. Impact of Support Properties. The most efficient Au-deposition method (DP) was used to study the influence of different TiO_2 phase compositions as support material: two mixed anatase/rutile materials (P25 and Hom), the pure phase supports anatase (Ana) and rutile (Rut) as well as an anatase/brookite composite (Bro) (see XRD patterns, Figure S10). Selected Au−TiO_2 catalysts were also synthesized via SIM and DP12 to investigate phase-dependent structural properties (see Supporting Information). Because the achieved Au loading was similar in all samples, the Au content on the surface was lower for supports with higher BET surface area as derived from XPS analysis (Table 5). Among all tested supports, the anatase/rutile mixed-phase supports, P25 and Hom, gave catalysts with the highest H_2 evolution rates (Table 5, Figure S11), independent of the chosen Au deposition method (Figure S12). As described above and in earlier works,[45b,47a,49] the higher activity with UV and visible light compared with the single phases anatase and rutile is probably based on a synergetic effect enabling efficient charge separation due to an additional electron transfer across the interface between the two TiO_2 phases anatase and rutile. Under visible light, it was shown that the "hot" Au electrons possess enough energy to be injected into the rutile conduction band, from which they are further transferred into the anatase phase,[45b,48] which may explain the superior vis activity of mixed anatase/rutile composites compared with the single phases, Rut and Ana.

Although the Rut support exhibits the highest surface area (96 m^2 g^{-1}), which is known to favor low recombination rates and therefore should improve the photocatalytic activity,[2] its H_2 production was quite poor compared with the other Au-loaded materials. In the in situ EPR spectrum of AuRut-DP, a signal of surface-bound $O_2^{\bullet-}$ radicals appeared under irradiation with UV−vis light (Figure 9). A weak Ti^{3+} signal (self-doped TiO_2) was already present in the dark. As described above, for the AuP25-DP12 catalyst, such Ti^{3+} species were formed during the Au deposition using DP at prolonged reaction times and may lower the efficiency of electron transfer between Au and TiO_2. This suggests that, probably because of the higher surface area, the Rut support was more sensitive to self-doping and related activity loss, whereas the same conditions did not cause such effects in the samples with lower surface area, based on P25 or Hom (Table 5, Figure 9). When Au was deposited onto Rut by the SIM method, which did not lead to self-doping, a higher H_2 production rate was observed (Figure S11).

In the case of the Ana support, the H_2 evolution rates under UV light were higher than those of the Rut catalyst. This is probably due to the lower sensitivity of Ana to self-doping, caused by the lower BET surface area. However, under visible light, no H_2 at all was formed (Table 5, Figure S11), regardless of which Au deposition method was used (Figure S12). Interestingly, in all samples based on P25, Hom, and Rut, strong EPR signals of $O_2^{\bullet-}$ were detected under irradiation with UV−vis light (Figure 9), but also with visible light (shown for AuP25-DP in Figure 8). In contrast, for catalyst AuAna-DP, which is not active with visible light, a weak $O_2^{\bullet-}$ signal is superimposed by a strong Ti^{3+} signal, with the principle values $g_{1,2}$ = 1.990 and g_3 = 1.962 of the anatase phase[34] (Figure 9, Table 3). This signal was present in all Ana-based materials (Figure S13), even without Au loading (not shown) and in the dark, showing neither light response nor changes due to addition of the reactants. Because XPS analysis did not indicate

Table 5. Catalyst Characterization of Au−TiO_2-DP with Different Support Materials

TiO_2 support	S_{BET}, m^2 g^{-1}	Au wt % (ICP−OES)	Au at. % (XPS)	H_2 evol. rate, mmol g^{-1} h^{-1} UV−vis	H_2 evol. rate, mmol g^{-1} h^{-1} vis	EPR species
P25	50	0.93	0.57	33	2.4	$O_2^{\bullet-}$
Hom	55	0.99	0.35	32	0.93	$O_2^{\bullet-}$
Rut	96	0.74	0.19	8.5[a]	0.37[a]	$O_2^{\bullet-}$
Ana	70	0.80	0.11	17[a]	0[a]	bulk Ti^{3+} (anatase)
Bro	77	0.85	0.16	11	0	bulk Ti^{3+} (anatase)

[a] Measured with 9.3 W irradiation (output).

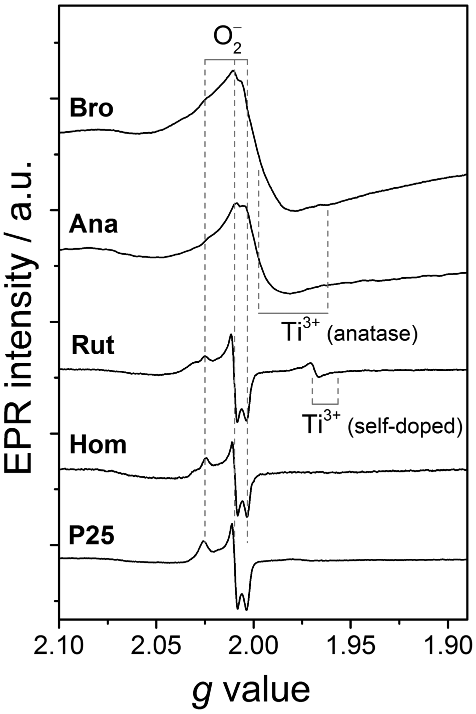

Figure 9. In situ EPR spectra of catalysts prepared with different TiO_2 support phases by the DP method measured after 20 min of UV−vis irradiation.

the presence of Ti^{3+} species on the surface of these samples, as in the case of AuP25-PD or AuP25-DP12, these intrinsic Ti^{3+} defects are probably already created during the TiO_2 synthesis and located in the bulk or subsurface region of the support. However, such defects might inhibit a sufficient SPR-induced charge transfer from Au to the TiO_2 support due to an increased Schottky barrier.

For the catalyst prepared with the anatase/brookite support (AuBro-DP), a similarly intense Ti^{3+} (anatase) signal was detected. Moreover, no H_2 evolution under visible light was observed, either with light above 420 nm or with a small UV contribution (Tables 5 and S2). However, its photoactivity under the full UV−vis range was appreciable (Table 5). Thus, the higher electron density resulting from the Ti^{3+} species in the Ana and Bro supports probably led to a negative shift of the anatase conduction band. This may be responsible for an increased Schottky barrier between Au and TiO_2 in these catalysts. Because the conduction band of brookite (E_{cb} = −0.46 V vs NHE)[37] is more negative than those of rutile and anatase, a transfer of the SPR-excited Au electrons into the brookite phase is likely to not occur.

4. CONCLUSIONS

We have shown that charge separation and transfer, initiated by ultraviolet or visible light in plasmonic Au−TiO_2 catalysts as well as the related H_2 evolution rates from H_2O/MeOH mixtures, depend greatly on the phase structure of the TiO_2 support and the method of gold deposition. In situ EPR spectroscopy proved to be a unique technique for visualizing light-induced separation and transport of charge carriers (electrons and holes) by detecting them as paramagnetic intermediates trapped at surface vacancies (electrons forming F centers) and surface OH groups (holes forming superoxide radicals).

Among the different support phases, anatase/rutile composites (P25 and Hom) provided the highest H_2 evolution rates with both UV−vis and visible light. This is likely caused by an improved charge separation due to an electron transfer across the anatase/rutile interface in both directions, depending on the excitation wavelength. In contrast, under visible light irradiation, no H_2 was evolved with gold supported on pure anatase or on the anatase/brookite composite with higher conduction band potentials. In situ EPR spectroscopy revealed an intrinsic accumulation of Ti^{3+} in the lattice of these supports, which may increase the Schottky barrier at the Au/TiO_2 interface and thereby hinders a sufficient SPR-promoted transfer of electrons from Au to TiO_2.

Among the different methods of gold deposition, short-term deposition−precipitation (DP) proved to be superior for two main reasons: (i) preferential trapping of photogenerated holes at specific surface-bound hydroxyl species (evidence from in situ EPR) promotes an effective reaction with the sacrificial reductant methanol, and (ii) uniform Au particles are formed in the early stages of the photocatalytic reaction (evidence from in situ UV−vis and XANES spectroscopy). Interestingly, even the small UV light contribution remaining in the experiments with a 400−700 nm filter (or under true solar radiation) is apparently sufficient to generate Au particles large enough to enable SPR-promoted electron transfer, from the Au particles to the TiO_2 conduction band excited by pure visible light. However, because this method was shown to be sensitive to the specific conditions, such as reaction time and support properties (e.g., BET surface area), care should be taken to select optimized reaction conditions. Sol immobilization led to slightly less active catalysts, possibly because of missing hole stabilization at surface OH groups and, thus, less effective charge separation. The latter property seems to be worst, at least under the conditions used in this work, for catalysts prepared by photodeposition (PD). These compounds showed the lowest H_2 evolution rates and almost no EPR signals of stabilized charge carriers.

Despite clear evidence that the SPR effect of Au particles is able to excite Au electrons for the reduction of protons[11a,20] and to initiate H_2 evolution exclusively with pure visible light ($\lambda > 420$ nm), the impact of this effect on its own is certainly not sufficient to produce amounts of H_2 being of practical relevance. However, a significant improvement seems to be possible in the presence of only a small percentage of UV light, as also contained in real sun light.

■ ASSOCIATED CONTENT

Ⓢ Supporting Information

The following file is available free of charge on the ACS Publications website at DOI: 10.1021/cs5018375.

> Radiation spectra of the light source used in the photocatalytic tests (Figure S1), H_2-evolution curves of the AuP25 catalysts (Figure S2), H_2 evolution of selected catalysts with light >420 nm (Table S1), XPS (Ti 2p) spectra of catalysts (Figure S3), UV−vis spectra of catalysts during and after the reaction (Figures S4 and S6), Au particle size distributions from TEM analysis of AuP25-DP after the reaction (Figure S5), in situ FTIR spectra of AuP25-SIM under vis and UV−vis light (Figure S7), FTIR spectra of catalysts (Figure S8), low-temperature in situ EPR spectra of calcined AuP25-DP (Figure S9), XRD patterns of catalysts (Figure S10),

photocatalytic H_2-evolution curves of catalysts with different supports and preparation methods (Figures S11 and S12), and in situ EPR spectra of catalysts with different supports and preparation methods (Figure S13) (PDF)

AUTHOR INFORMATION

Corresponding Author

*E-mail: angelika.brueckner@catalysis.de.

Present Addresses

[†](M. Karnahl) University of Stuttgart, Institute of Organic Chemistry, Pfaffenwaldring 55, 70569 Stuttgart, Germany.
[§](J. B. Priebe) Leibniz-Institut für Plasmaforschung and Technologie e.V., Felix-Hausdorff-Straße 2, 17489 Greifswald, Germany.

Notes

The authors declare no competing financial interest.

ACKNOWLEDGMENTS

The authors thank the Deutsche Forschungsgemeinschaft (DFG-SPP1613) for financial support. A.J.J.L. thanks the Alexander von Humboldt foundation for funding. We thank M. Sebek and S. Schüler for their help with the catalyst preparations; P. Bartels for the conduction of photocatalytic tests; and A. Bellmann, S. Ahlers, M. Schneider, and C. Kreyenschulte for their contributions to the catalyst characterization. For the XANES measurements, we thank U. Reinholz and F. Emmerling (Federal Institute of Material Research and Testing, Berlin) and the BESSY staff.

REFERENCES

(1) Lewis, N. S.; Nocera, D. G. *Proc. Natl. Acad. Sci. U.S.A.* **2006**, *103*, 15729−15735.

(2) Kudo, A.; Miseki, Y. *Chem. Soc. Rev.* **2009**, *38*, 253−278.

(3) (a) Yuan, J.; Chen, M.; Shi, J.; Shangguan, W. *Int. J. Hydrogen Energy* **2006**, *31*, 1326−1331. (b) Mohapatra, S. K.; Misra, M.; Mahajan, V. K.; Raja, K. S. *J. Phys. Chem. C* **2007**, *111*, 8677−8685.

(4) (a) Kato, H.; Kudo, A. *J. Phys. Chem. B* **2002**, *106*, 5029−5034. (b) Choi, W.; Termin, A.; Hoffmann, M. R. *J. Phys. Chem.* **1994**, *98*, 13669−13679.

(5) Irie, H.; Watanabe, Y.; Hashimoto, K. *J. Phys. Chem. B* **2003**, *107*, 5483−5486.

(6) Serpone, N.; Emeline, A. *J. Phys. Chem. Lett.* **2012**, *3*, 673−677.

(7) (a) Zheng, Z.; Huang, B.; Qin, X.; Zhang, X.; Dai, Y.; Whangbo, M. H. *J. Mater. Chem.* **2011**, *21*, 9079−9087. (b) Zielińska-Jurek, A.; Kowalska, E.; Sobczak, J. W.; Lisowski, W.; Ohtani, B.; Zaleska, A. *Appl. Catal., B* **2011**, *101*, 504−514. (c) Orlov, A.; Chan, M.; Jefferson, D.; Zhou, D.; Lynch, R.; Lambert, R. *Environ. Technol.* **2006**, *27*, 747−752.

(8) (a) Naya, S.-i.; Teranishi, M.; Isobe, T.; Tada, H. *Chem. Commun.* **2010**, *46*, 815−817. (b) Ke, X.; Sarina, S.; Zhao, J.; Zhang, X.; Chang, J.; Zhu, H. *Chem. Commun.* **2012**, *48*, 3509−3511.

(9) (a) Gomes Silva, C.; Juárez, R.; Marino, T.; Molinari, R.; García, H. *J. Am. Chem. Soc.* **2011**, *133*, 595−602. (b) Tanaka, A.; Sakaguchi, S.; Hashimoto, K.; Kominami, H. *Catal. Sci. Technol.* **2012**, *2*, 907−909. (c) Gallo, A.; Marelli, M.; Psaro, R.; Gombac, V.; Montini, T.; Fornasiero, P.; Pievo, R.; Dal Santo, V. *Green Chem.* **2012**, *14*, 330−333.

(10) (a) Hollmann, D.; Gärtner, F.; Ludwig, R.; Barsch, E.; Junge, H.; Blug, M.; Hoch, S.; Beller, M.; Brückner, A. *Angew. Chem., Int. Ed.* **2011**, *50*, 10246−10250. (b) Kessler, M.; Schueler, S.; Hollmann, D.; Klahn, M.; Beweries, T.; Spannenberg, A.; Brückner, A.; Rosenthal, U. *Angew. Chem., Int. Ed.* **2012**, *51*, 6272−6275.

(11) (a) Priebe, J. B.; Karnahl, M.; Junge, H.; Beller, M.; Hollmann, D.; Brückner, A. *Angew. Chem., Int. Ed.* **2013**, *52*, 11420−11424. (b) Meyer, T.; Priebe, J. B.; da Silva, R. O.; Peppel, T.; Junge, H.; Beller, M.; Brückner, A.; Wohlrab, S. *Chem. Mater.* **2014**, *26*, 4705−4711.

(12) (a) Kowalska, E.; Mahaney, O. O. P.; Abe, R.; Ohtani, B. *Phys. Chem. Chem. Phys.* **2010**, *12*, 2344−2355. (b) Nadeem, M.; Murdoch, M.; Waterhouse, G.; Metson, J.; Keane, M.; Llorca, J.; Idriss, H. *J. Photochem. Photobiol., A* **2010**, *216*, 250−255.

(13) (a) Bamwenda, G. R.; Tsubota, S.; Nakamura, T.; Haruta, M. *J. Photochem. Photobiol., A* **1995**, *89*, 177−189. (b) Carneiro, J. T.; Yang, C.-C.; Moma, J. A.; Moulijn, J. A.; Mul, G. *Catal. Lett.* **2009**, *129*, 12−19. (c) Murdoch, M.; Waterhouse, G.; Nadeem, M.; Metson, J.; Keane, M.; Howe, R.; Llorca, J.; Idriss, H. *Nat. Chem.* **2011**, *3*, 489−492. (d) Veith, G. M.; Lupini, A. R.; Dudney, N. J. *J. Phys. Chem. C* **2008**, *113*, 269−280.

(14) Tomita, K.; Petrykin, V.; Kobayashi, M.; Shiro, M.; Yoshimura, M.; Kakihana, M. *Angew. Chem., Int. Ed.* **2006**, *45*, 2378−2381.

(15) Gärtner, F.; Losse, S.; Boddien, A.; Pohl, M. M.; Denurra, S.; Junge, H.; Beller, M. *ChemSusChem* **2012**, *5*, 530−533.

(16) (a) Di Paola, A.; Marci, G.; Palmisano, L.; Schiavello, M.; Uosaki, K.; Ikeda, S.; Ohtani, B. *J. Phys. Chem. B* **2002**, *106*, 637−645. (b) Su, R.; Tiruvalam, R.; He, Q.; Dimitratos, N.; Kesavan, L.; Hammond, C.; Lopez-Sanchez, J. A.; Bechstein, R.; Kiely, C. J.; Hutchings, G. J. *ACS Nano* **2012**, *6*, 6284−6292.

(17) Haruta, M. *Gold Bull.* **2004**, *37*, 27−36.

(18) Kandiel, T. A.; Ivanova, I.; Bahnemann, D. W. *Energy Environ. Sci.* **2014**, *7*, 1420−1425.

(19) Subramanian, V.; Wolf, E. E.; Kamat, P. V. *J. Am. Chem. Soc.* **2004**, *126*, 4943−4950.

(20) Qian, K.; Sweeny, B. C.; Johnston-Peck, A. C.; Niu, W.; Graham, J. O.; DuChene, J. S.; Qiu, J.; Wang, Y.-C.; Engelhard, M. H.; Su, D.; Stach, E. A.; Wei, W. D. *J. Am. Chem. Soc.* **2014**, *136*, 9842−9845.

(21) Tian, Y.; Tatsuma, T. *J. Am. Chem. Soc.* **2005**, *127*, 7632−7637.

(22) Linic, S.; Christopher, P.; Ingram, D. B. *Nat. Mater.* **2011**, *10*, 911−921.

(23) Porta, F.; Prati, L.; Rossi, M.; Coluccia, S.; Martra, G. *Catal. Today* **2000**, *61*, 165−172.

(24) Satoh, N.; Hasegawa, H.; Tsujii, K.; Kimura, K. *J. Phys. Chem.* **1994**, *98*, 2143−2147.

(25) Casaletto, M.; Longo, A.; Martorana, A.; Prestianni, A.; Venezia, A. *Surf. Interface Anal.* **2006**, *38*, 215−218.

(26) Ascarelli, P.; Cini, M.; Missoni, G.; Nistico, N. *J. Phys. Colloques* **1977**, *38*, C2−125-C2−128.

(27) Schumacher, B.; Plzak, V.; Cai, J.; Behm, R. *Catal. Lett.* **2005**, *101*, 215−224.

(28) Zanella, R.; Delannoy, L.; Louis, C. *Appl. Catal., A* **2005**, *291*, 62−72.

(29) Jiang, Z.; Zhang, W.; Jin, L.; Yang, X.; Xu, F.; Zhu, J.; Huang, W. *J. Phys. Chem. C* **2007**, *111*, 12434−12439.

(30) Gong, X.-Q.; Selloni, A.; Dulub, O.; Jacobson, P.; Diebold, U. *J. Am. Chem. Soc.* **2008**, *130*, 370−381.

(31) (a) Fierro-Gonzalez, J. C.; Guzman, J.; Gates, B. C. *Top. Catal* **2007**, *44*, 103−114. (b) Yang, J. H.; Henao, J. D.; Raphulu, M. C.; Wang, Y.; Caputo, T.; Groszek, A.; Kung, M. C.; Scurrell, M. S.; Miller, J. T.; Kung, H. H. *J. Phys. Chem. B* **2005**, *109*, 10319−10326. (c) Henao, J. D.; Caputo, T.; Yang, J. H.; Kung, M. C.; Kung, H. H. *J. Phys. Chem. B* **2006**, *110*, 8689−8700.

(32) Dimitrijevic, N. M.; Saponjic, Z. V.; Rabatic, B. M.; Poluektov, O. G.; Rajh, T. *J. Phys. Chem. C* **2007**, *111*, 14597−14601.

(33) (a) Zuo, F.; Wang, L.; Wu, T.; Zhang, Z.; Borchardt, D.; Feng, P. *J. Am. Chem. Soc.* **2010**, *132*, 11856−11857. (b) Xing, M.; Fang, W.; Nasir, M.; Ma, Y.; Zhang, J.; Anpo, M. *J. Catal.* **2013**, *297*, 236−243. (c) Okumura, M.; Coronado, J. M.; Soria, J.; Haruta, M.; Conesa, J. C. *J. Catal.* **2001**, *203*, 168−174.

(34) Coronado, J. M.; Maira, A. J.; Conesa, J. C.; Yeung, K. L.; Augugliaro, V.; Soria, J. *Langmuir* **2001**, *17*, 5368−5374.

(35) Howe, R. F.; Grätzel, M. *J. Phys. Chem.* **1987**, *91*, 3906−3909.

(36) Li, Z.; Dong, T.; Zhang, Y.; Wu, L.; Li, J.; Wang, X.; Fu, X. *J. Phys. Chem. C* **2007**, *111*, 4727−4733.

(37) Di Paola, A.; Bellardita, M.; Ceccato, R.; Palmisano, L.; Parrino, F. *J. Phys. Chem. C* **2009**, *113*, 15166−15174.
(38) Wardman, P. *J. Phys. Chem. Ref. Data* **1989**, *18*, 1637−1755.
(39) Dung, D.; Ramsden, J.; Graetzel, M. *J. Am. Chem. Soc.* **1982**, *104*, 2977−2985.
(40) Sawyer, D. T.; Valentine, J. S. *Acc. Chem. Res.* **1981**, *14*, 393−400.
(41) Anpo, M.; Che, M.; Fubini, B.; Garrone, E.; Giamello, E.; Paganini, M. C. *Top. Catal* **1999**, *8*, 189−198.
(42) Villarreal, T. L.; Gomez, R.; Neumann-Spallart, M.; Alonso-Vante, N.; Salvador, P. *J. Phys. Chem. B* **2004**, *108*, 15172−15181.
(43) Primo, A.; Corma, A.; García, H. *Phys. Chem. Chem. Phys.* **2011**, *13*, 886−910.
(44) Park, E. D.; Lee, J. S. *J. Catal.* **1999**, *186*, 1−11.
(45) (a) Akita, T.; Lu, P.; Ichikawa, S.; Tanaka, K.; Haruta, M. *Surf. Interface Anal.* **2001**, *31*, 73−78. (b) Tsukamoto, D.; Shiraishi, Y.; Sugano, Y.; Ichikawa, S.; Tanaka, S.; Hirai, T. *J. Am. Chem. Soc.* **2012**, *134*, 6309−6315.
(46) Tsubota, S.; Cunningham, D.; Bando, Y.; Haruta, M. *Stud. Surf. Sci. Catal.* **1995**, *91*, 227−235.
(47) (a) Hurum, D. C.; Agrios, A. G.; Gray, K. A.; Rajh, T.; Thurnauer, M. C. *J. Phys. Chem. B* **2003**, *107*, 4545−4549. (b) Hurum, D.; Agrios, A.; Crist, S.; Gray, K.; Rajh, T.; Thurnauer, M. *J. Electron. Spectrosc.* **2006**, *150*, 155−163.
(48) Scanlon, D. O.; Dunnill, C. W.; Buckeridge, J.; Shevlin, S. A.; Logsdail, A. J.; Woodley, S. M.; Catlow, C. R. A.; Powell, M. J.; Palgrave, R. G.; Parkin, I. P. *Nat. Mater.* **2013**, *12*, 798−801.
(49) (a) Komaguchi, K.; Nakano, H.; Araki, A.; Harima, Y. *Chem. Phys. Lett.* **2006**, *428*, 338−342. (b) Kawahara, T.; Konishi, Y.; Tada, H.; Tohge, N.; Nishii, J.; Ito, S. *Angew. Chem., Int. Ed.* **2002**, *114*, 2935−2937.